

Lossy Event Compression based on Image-derived Quad Trees and Poisson Disk Sampling

Srutarshi Banerjee Zihao W. Wang Henry H. Chopp,
Oliver Cossairt Aggelos K. Katsaggelos
Northwestern University

srutarshibanerjee2022@u.northwestern.edu

Abstract

With several advantages over conventional RGB cameras, event cameras have provided new opportunities for tackling visual tasks under challenging scenarios with fast motion, high dynamic range, and/or power constraint. Yet unlike image/video compression, the performance of event compression algorithm is far from satisfying and practical. The main challenge for compressing events is the unique event data form, i.e., a stream of asynchronously fired event tuples each encoding the 2D spatial location, timestamp, and polarity (denoting an increase or decrease in brightness). Since events only encode temporal variations, they lack spatial structure which is crucial for compression. To address this problem, we propose a novel event compression algorithm based on a quad tree (QT) segmentation map derived from the adjacent intensity images. The QT informs 2D spatial priority within the 3D space-time volume. In the event encoding step, events are first aggregated over time to form polarity-based event histograms. The histograms are then variably sampled via Poisson Disk Sampling prioritized by the QT based segmentation map. Next, differential encoding and run length encoding are employed for encoding the spatial and polarity information of the sampled events, respectively, followed by Huffman encoding to produce the final encoded events. Our Poisson Disk Sampling based Lossy Event Compression (PDS-LEC) algorithm performs rate-distortion based optimal allocation. On average, our algorithm achieves greater than $6\times$ higher compression compared to the state of the art.

1. Introduction

Inspired by biological visual systems, event cameras are novel sensors designed to capture visual information with a data form drastically different from traditional images and videos [38, 27]. The event pixels do not directly output the intensity signals as traditional cameras do. Instead,

each pixel compares the difference between the current log-intensity state and the previous state, and fires an event when the difference exceeds the firing positive or negative thresholds. This sensing mechanism provides several benefits. First, event pixels operate independently which enables very low latency ($\sim 10\mu\text{s}$) and therefore high speed imaging. Second, event cameras have high dynamic range (HDR, $\sim 120\text{dB}$) compared to regular frame-based cameras ($\sim 60\text{dB}$). Third, the events reduce redundant captures of static signals. Last, event cameras consume lower power (10mW) than traditional cameras ($\sim 1\text{W}$). As such, event cameras have brought new solutions to many classical as well as novel problems in computer vision and robotics, including high frame-rate video reconstruction [46, 34, 37], with HDR [43, 33] and high resolution [44, 28, 45], and 3D reconstruction of human motion [49] and scenes [31, 23], as well as odometry [11, 41] and tracking [52, 24].

Currently, events are mainly communicated in the raw format using the Address Event Representation (AER) protocol [1]. The current AER protocol, AEDAT 4.0, released in July 2019, [1] uses 96 bits representation for each event tuple (x, y, t, p) which are (x, y) position, timestamp and polarity, while its earlier version, AEDAT 3.1, uses 64 bit representation for each event. The timestamp uses the most bits due to its resolution with 64 bits and 32 bits for AEDAT 4.0 and AEDAT 3.1, respectively. Although AEDAT 4.0 has incorporated lossless encoding standards such as LZ4, LZ4_HIGH, ZSTD and ZSTD_HIGH [1], effective lossy event encoding has not been proposed in the literature or implemented in the event cameras.

In traditional image/video compression standards, lossy compression is achieved by exploiting the spatial and temporal correlations. However, events are discrete points scattered in the space-time volume (see, for example Fig. 1 left). Several prior works have approached event compression [8, 16, 21]. TALVEN [21] has aimed at aggregating events based on event timestamps. While this improves the compression ratio (CR), the benefits of high compression is only evident when aggregating events over a long time du-

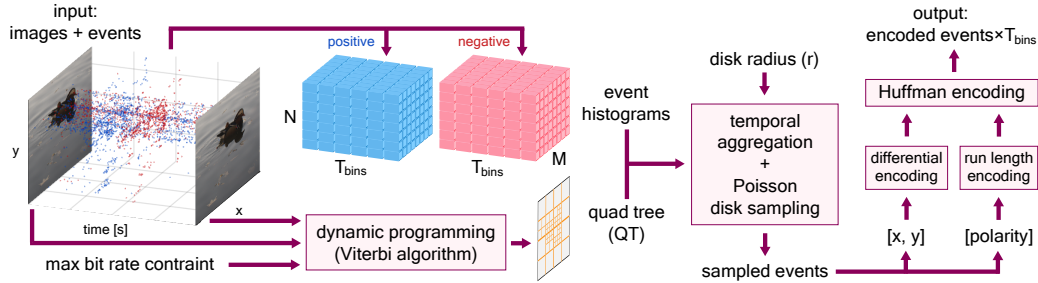


Figure 1: Overall Architecture of the PDS-LEC

ration (e.g., $> 20ms$), which in turn reduces the advantages of events.

Our goal is to design an efficient event compression algorithm that exploits the spatio-temporal redundancy of events without sacrificing temporal information. Our approach considers the hybrid input of RGB images and events, which is a context largely existing in the literature [53, 29, 45, 41]. We reason that the adjacent in time images have rich spatial features that can be leveraged to guide event compression. Therefore, we first compute a quad tree (QT) structure to serve as the priority map. Note that the QT can be generated from events as well. Next, the events are sampled to generate a blue noise distribution locally with the QT defining regions of importance, albeit in 2D space. The blue noise pattern of events is generated by Poisson Disk Sampling (PDS) [10] which randomly samples events. The overall framework is shown in Fig. 1. In particular, this paper makes the following contributions:

(1) We propose a novel algorithm for lossy compression of neuromorphic events based on the QT segmentation map from adjacent images exploiting spatio-temporal redundancy.

(2) We evaluate our approach qualitatively and quantitatively, on existing event datasets and compare our results with state of art and other techniques.

2. Related Work

Conventional image and video based coding techniques have evolved over the last couple of decades which led to a successful telecom revolution globally. Several standards came out as a result of the persistent effort, some of the latest video standards being HEVC, H.264, AVS2, VP9 [39, 48, 19, 30]. With images and videos, the 2D and/or 3D spatio-temporal consistency of the data is exploited to have an efficient coding algorithm. However, events are asynchronous and non-continuous in space and time. Limited work [16, 8] has been done in predicting the distribution of events in space, time and polarity.

2.1. DVS Coding Approaches

The approaches for compressing DVS data can be classified into two categories: (a) specifically encoding events, (b) applying existing methods to events.

A. DVS Specific Coding

(1) *Spike Coding*: Lossless event compression was first proposed in [8]. The encoding was derived from a spike firing model exploiting spatial and temporal correlation. The events are projected into a sequence of three-dimensional macro-cubes and encoded using Address-Prior (AP) and Time-Prior (TP) modes. The AP mode is designed for scenarios where events are scattered all over the 2D space, while the TP mode is designed for cases where events occur locally. The residuals are encoded using arithmetic coding (CABAC). The authors extended this algorithm to include intercubes prediction utilizing the temporal correlation among microcubes [16], although the compression ratio did not improve significantly.

(2) *TALVEN*: The time aggregation strategy based lossless video encoding strategy was devised in [21]. The events are time-aggregated into an event frame with a histogram count at each pixel location where each event frame is separated based on event polarities. The concatenated frames are coded using conventional lossless video encoding techniques including interframe coding, intraframe coding and entropy coding (CABAC) with the data packets incorporated into Network Abstraction Layer (NAL) units. The CR of this technique is significantly higher than the Spike Coding especially at higher time aggregation.

B. Existing compression methods for Events

The application of existing compression methods tailored to events can be broadly categorized into:

(1) *Entropy coding* - Entropy coders like Huffman and arithmetic coding can potentially be applied to events [18] considering each event field (x, y, t, p) as separate symbols. The gains of using just this technique are rather limited.

(2) *Dictionary based compression* - A collection of long strings and shorter codewords is maintained in a dictionary data structure. Advanced dictionary coders Zstd [2], Zlib

[14], LZ77 [54], LZMA [3] and Brotli [6] utilize multi-level encoding to improve compression ratios.

(3) *IoT specific compression* - An Internet of Things (IoT)-specific strategy has been devised for resource constrained devices [9] without violating memory and latency constraints of the IoT devices. Sprintz exploits correlations among successive samples of a multivariate stream. The event stream can be directly converted to a multivariate time series data for compression. This strategy works better when it is required to have higher compression gains with reduced power consumption [18].

(4) *Fast integer compression* - In order to boost up the encoding and decoding speed (e.g. billions of arrays of integers for search engines), fast integer compression is often the choice. Simple8B [9], Memcpy [9], SIMD-BP128 [26], FastPFOR [26] and SNAPPY [4] are some of the fast integer compression algorithms. When DVS data needs a rapid data transfer, fast integer compression can be applied by transforming events into vectors.

A comparison of these approaches has been done in [20, 21] resulting in low compression ratios between 1 and 4. The aforementioned approaches do not consider spatio-temporal encoding of events at the same time.

2.2. Blue Noise Sampling

Blue noise based sampling is widely applied in rendering, texturing, animation and related domains. Blue noise captures the local density of the image through its local point density. It has isotropic properties which lead to high-quality sampling of multidimensional signals without any aliasing [25]. Blue noise distribution has been generated over the years by several techniques—error diffusion [40, 17], dart throwing algorithm [12]—to create Poisson disk distributions and other techniques. Poisson disk algorithms that generate blue noise samples [50, 13, 47, 42, 51, 15] by reducing the computational complexity and improving the blue noise characteristics are widely studied and applied in the field of computer graphics.

We leverage a fast Poisson Disk Sampling (PDS) technique as a method to sample events in 2D space. This generates a blue noise pattern preserving the high frequency spectral components of the events. We compare PDS with random sampling in Section 6 and show that using PDS results in overall higher compression ratio and better event compression metrics.

3. Spatio-Temporal Event Compression

Mathematical analysis in [8, 16] points out the correlation of DVS spikes in both space and time. The adjacent pixels receive the same illumination change (increase or decrease) over time. This leads to spatial as well as temporal correlation in local regions. We exploit this fundamental nature of the DVS spikes for encoding events. First, we

generate a quad tree (QT) structure from the adjacent intensity frame which indicates spatial priority regions. Depending on the block sizes, we develop a strategy based on Poisson disk sampling for removing events based on spatio-temporal proximity to each other. The events are encoded based on block sizes using entropy encoding strategies. In the following subsections, the framework is described in more details.

3.1. Generation of Quadtree (QT) structure

The events are generated due to scene complexity (edges/textures of the objects in scene) and (or) relative motion of the camera with respect to the scene. Khan *et al.* [22] showed that the event rate depends exponentially on the scene complexity metric and linearly on the sensor speed metric. However, the scene complexity provides us with the important events pertaining to objects.

We rely on the intensity frames to generate the priority regions for the events. Although priority can be generated in different ways, in this work we use the QT data structure in order to divide the frame into blocks. The QT can subdivide the frames into different levels resulting in heterogeneous blocks of sizes determined by the leaf level of the QT. Larger block sizes indicate lower priority regions while smaller blocks indicate higher priority. A time aggregated event stream between two successive intensity frames can be approximated by a difference of these intensity frames. Hence, the priority regions for events is proportional to the difference between these intensity frames. We generate the QT based on the system described in [7]. For an event volume E_{t-1} , between successive intensity frames \hat{I}_{t-1} and I_t (both as defined in [7]), we leverage on these intensity frames to derive a relevant QT structure. The QT is generated using Dynamic Programming (Viterbi optimization [36]) which provides a trade-off between the frame distortion (D) and frame bit rate (R). This is done by minimizing D over the leaves of the QT, denoted by \mathbf{x} , subject to a given maximum bit rate R_{max} . In other words, we are solving for the rate-distortion tradeoff for the intensity frames. The constrained discrete optimization is solved using Lagrangian relaxation, leading to solutions in the convex hull of the rate-distortion curve. The Lagrangian cost function is of the form

$$J_\lambda(\mathbf{x}) = D(\mathbf{x}) + \lambda R(\mathbf{x}), \quad (1)$$

where $\lambda \geq 0$ is a Lagrangian multiplier. The intensity bit rate is set to be generated for a fixed rate (within a tolerance) constraint. The QT is generated such that the intensity bit rate satisfies this constraint. λ is adjusted at each frame for achieving the desired bit rate. The optimal λ^* is computed by a convex search in the Bezier curve [36] over the rate-distortion space which results in convergence in fewer iterations. The optimal QT segmentation map corresponds

to λ^* and at a set bit rate, satisfies equation (S1), derived for intensity frame I_t based on the distorted frame \hat{I}_{t-1} . Clearly, at higher bit rates the QT can go to deeper levels (and hence smaller blocks) while for smaller bit rates, the QT branches out to shallow levels. This 2D segmentation map is applied to the event volume E_{t-1} providing regions of priority for event compression, with block size inversely proportional to the priority in the block.

3.2. Poisson Disk Sampling

The QT structure provides a segmentation map. Since the events are correlated locally in space and time, there exists local redundancy not only in the temporal dimension but also in the spatial dimensions. The local region in space is quite abstract as it may vary from scene to scene and also within a scene. In this work, the QT block sizes indicate the importance of the regions, which is also an indication of the dimensions of local regions in space-time. There could be local features in bigger blocks, but these are not of high priority based on the set bit rate on intensity frames.

We perform lossy compression on events not only by sampling the events from the QT blocks, but also temporally aggregating the events. Sampling of events inside the QT blocks is challenging due to the presence of both local structure and noise. There may be aggregation of events at object edges, which may be increased due to presence of noise in the sensor. The events are sampled as a blue noise pattern. The blue noise pattern picks up the local event density without adding any inherent artificial structures. This leads to high-quality sampling of multi-dimensional signals while preventing aliasing. In this work, PDS is used to generate blue noise.

PDS is applied on the events inside the QT blocks. PDS sample events, with all events at least r distance apart from each other. Bridson [10] proposed a fast PDS strategy in multidimensional space. However, the algorithm would generate points in space based on the PDS. In our work, we sample events based on this PDS technique. The resulting sampled events are generated with at least r distance apart from each other. Given M original events, we sample R_e events, where $R_e \leq M$. PDS can be applied on the whole event volume or on regions of the events. Since the QT already provides us with a priority map, PDS is done with different r on blocks of different sizes in the QT.

PDS needs a reference position to start sampling the events. In a QT block, it is difficult to identify a reference starting point for PDS. The reference starting point can be conveniently in any of the corner locations in the QT block (or any other location in the QT block). However, this might lead to a reference point which may not have an event. In order to eliminate any such issues, we consider the reference point as the location of the event at or nearest to the centroid (geometric median) with respect to the event loca-

tions in a QT block. Thus, in a neighborhood of $N \times N$ pixels, we find the geometric median x_m , of the M events, as shown in Eqn. (2), where each $x_i \in \mathbb{R}^n$ are the event locations in space-time.

$$x_m = \arg \min_{x_m} \sum_{i=1}^M \|x_i - x_m\|_2, \quad (2)$$

Except for the chosen point, we do not sample the events lying within a disk of radius r , with respect to this reference point. Next, we shift our reference point to the nearest event location outside the radius r and do not sample the events lying within radius r (termed as Poisson Disk Radius (PDR)) with respect to this new reference point. This step is repeated until all the events are at least or greater than a spatial distance r from each other. This sampling strategy has the effect of sampling the event density locally in the region of $N \times N$ pixels, along with introducing a fixed spatial sampling pattern in the event volume. The sampling approach not only reduces the density of the aggregated events near the edges but can also remove the uncorrelated noisy events from local regions in space.

3.3. Lossy Event Compression

The QT provides the priority map and PDS provides an efficient strategy to reduce the density of events and noise from the events. However, the QT has different sized blocks which indicate different priorities. We want to sample events based on priority as this will retain local features in high priority regions and remove local features from lower priority regions. This is achieved by using different Poisson disk radius r values for different QT block sizes: higher and smaller r values for bigger and smaller QT blocks, respectively. In our algorithm, we specifically apply PDS to blocks larger than 2×2 . For QT block sizes below 4×4 , we do not sample events as we consider those blocks to be regions of very high priority and hence all events in those regions are critical. As mentioned in subsection 3.1, we obtain the QT for event volume E_{t-1} from reconstructed intensity frame \hat{I}_{t-1} and actual frame I_t .

The lossy event compression is performed in steps depending on the bandwidth available for communication between network-connected IoT devices. The lossy event compression framework has a lossy part as well as a lossless part. The lossy portion of event encoding consists of 2 parts: (a) quantizing (aggregating) event timestamps as T_{bin} and (b) PDS of the events with spatial overlap of event (x, y) locations within the QT blocks. In step (a), we compute the histogram for the positive and negative events separately for each quantized timestamp. The lossless portion of the event encoding involves differentially encoding the (x, y) location of events followed by Huffman coding. The polarity is encoded by Run Length Encoding (RLE) fol-

Algorithm 1: Event Compression Pseudo Code

Input: Adjacent Intensity frames, Event Volume
set $\lambda_{min}, \lambda_{max}, R_{max}$;
while intensity bit rate $R > R_{max}$ **do**
| adjust λ to obtain desired R as in Sec. 3.1
end
Result: Optimal QT
set T_{bin} and r_4 ;
Aggregate events into event histogram frames
(positive and negative) based on T_{bin} ;
while QT blocks $\in \{ 4 \times 4, 8 \times 8 \text{ and higher} \}$ **do**
| compute the centroid C of events in (x, y) ;
| Shift C to nearest event location P (if $C \neq P$);
if events left to be visited **then**
| Remove events within radius r_i from P ;
| set P as nearest event outside r_i ;
end
| Encode (x, y) differentially followed by
| Huffman coding for each block;
| Encode event counts as Run Length Encoding
| each block followed by Huffman coding;
end
while QT blocks $\in \{ 2 \times 2 \}$ **do**
| Encode (x, y) differentially each block;
| Encode event counts as Run Length Encoding
| each block followed by Huffman coding;
end
while QT blocks $\in \{ 1 \text{ pixel} \}$ **do**
| Consider all pixels in the frame;
| Encode event counts as Run Length Encoding
| followed by Huffman coding;
end
Output: Compressed Event Volume

lowed by Huffman encoding (HE). The quantized (aggregated) timestamps for the events form the basis of aggregating events as subframes corresponding to that timestamp. For each timestamp, there are 2 subframes - one for positive and one for negative events. These events are grouped together as a frame before transmission/storage. The algorithm is mentioned in detail in Algorithm 1 with overall architecture shown in Fig. 1. It must be clearly stated that we are developing a heuristics based rule for compressing the events. This algorithm offers flexibility in terms of event compression. Depending on the desired bitrate, the event compression may be set by the user, by varying r and T_{bin} .

4. Experiments

4.1. Dataset

In order to show the benefits of the proposed lossy compression strategy, we use datasets available in the literature which have both intensity frames and events. Sequences

from RGB-DAVIS dataset [45, 5] are used to show the compression performance in different settings for image reconstruction experiments. The Dynamic and Active-pixel Vision Sensor (DAVIS) dataset [29] is used to show a comparison of PDS-LEC with other state-of-the-art event compression algorithms. Shapes-6dof, Dynamic-6dof, Slider-depth, Outdoors Running sequence has been used in DAVIS dataset. Running1 and Running2 sequences has been derived from Outdoors Running as done in [21].

4.2. Event Compression Metric

(a) **Event Distortion Metric:** The compressed events essentially represent the original 3D spatio-temporal event volume in a quantized manner. However, the fidelity of the compressed events with respect to undistorted event volume is very important to understand the level of distortion. In this direction, to the best of our knowledge, there is no metric for computing event distortion and we are making a first attempt in quantizing the distortion. The event spatial location (x, y) is not only important, but the timestamp is also a vital parameter for various event based processing algorithms. The distortion of the events in both the spatial and temporal aspects must be computed.

We separate the spatial and temporal fidelity of the distorted event volume with respect to the undistorted events in order to have a complete understanding of the role of different parameters in encoding events. For computing the spatial distortion, we aggregate the events over the time bins into an (x, y) event image. The PSNR and SSIM metrics computed on the aggregated compressed and uncompressed event images are used for computing the spatial distortion. The temporal distortion is rather hard to quantify. We define a temporal error metric to quantify the quantization error in time as described in Eqn. 3:

$$T_{error} = \frac{1}{N_{fr}} \sum_{i=1}^{N_{fr}} \sqrt{\sum_j (T_{j,org} - T_{j,quant})^2}, \quad (3)$$

where N_{fr} is the number of event volumes in a sequence, $T_{j,org}$ is the timestamp of j^{th} event in i^{th} frame, and $T_{j,quant}$ is the quantized timestamp of j^{th} event in a compressed i^{th} frame. Based on the end application of events, a weighted distortion metric may be computed with weights w_s and w_t for spatial distortion D_s and temporal distortion D_t , respectively, thereby prioritizing spatial and / or temporal distortions differently.

(b) **End-to-End Event Compression Metric:** We also compute the end-to-end compression ratio for the events [21], considering 64 bits for each event. The compression ratio is given by the ratio of uncompressed events and the encoded event bit representation.

$$Ev_{comp} = \frac{\text{Bits/event} \times N_{events}}{\gamma}, \quad (4)$$

where γ is the compressed event bits.

5. Performance of proposed framework

Here we show a performance study of the proposed lossy event compression framework with respect to different compression parameters.

5.1. Performance with varying T_{bin} only

In one of the experiments, the QT segmentation is not used. The events are not sampled based on Poisson disk sampling. However, the events are temporally aggregated into N bins, with $N \in \{8, 16, 24\}$. To quantify the benefits of the temporal compression, we compute the compression ratio of the original uncompressed events as well as the compressed events. Table 1 shows the compression ratio and the average T_{error} over the sequence. Clearly, it can be

Sequence	T_{error}			CR (bit rate ratio)		
	8	16	24	8	16	24
Indoor3	0.269	0.134	0.089	1029.63	944.44	890.41
Indoor4	0.139	0.069	0.046	279.34	263.13	251.18
Indoor6	0.278	0.139	0.093	1643.04	1500.79	1371.94
Indoor9	0.341	0.166	0.113	3331.48	2643.58	2404.56
Outdoor5	0.149	0.076	0.051	41.84	40.68	39.65
Outdoor6	0.256	0.129	0.086	514.35	490.17	466.52
Outdoor9	0.183	0.089	0.062	45.03	44.23	43.46

Table 1: Temporal binning only. CR: compression ratio

seen that with the increase in the number of T_{bin} , the compression ratio reduces along with the reduction of T_{error} . Fig. 2(a) shows the original events while Figs. 2(b), (c) and (d) show the variation of events in temporal space with 8, 16 and 24 quantized timestamps respectively. The SSIM in this case is 1, since all events are sampled.

5.2. Performance with varying Intensity Bit Rate

The QT is optimized for particular operational bit rate for intensities only. In these experiments, $r_4 = 1$, $r_8 = 2r_4$, $r_{16} = 3r_4$ and $r_{32} = 4r_4$ with $T_{bin} = 16$ is used. The performance table is shown in Table 2. As bit rate reduces, the PSNR and SSIM reduces, while T_{error} and CR increases. This indicates bigger blocks in the QT for lower bit rates with considerably higher distortion. Sample event frames at varying intensity bit rate is shown in Fig. 2 (row 2).

5.3. Performance with varying Poisson Disk Radius and Temporal Binning

In this experiment, the performance of the event compression system is evaluated at a particular bit rate, but the Poisson disk radius r_4 is varied. As in section 5.2, $r_8 = 2r_4$, $r_{16} = 3r_4$ and $r_{32} = 4r_4$. The temporal binning of $T_{bin} = 16$ is used in this experiment. The PSNR and SSIM reduces as r_4 increases as shown in Table 3. The T_{error}

Sequence	Bit Rate (Mbps)	PSNR (dB)	SSIM	T_{error}	CR (bit rate)
Indoor3	0.5	43.07	0.9999	0.177	994.41
	0.3	41.71	0.9999	0.197	1048.16
	0.1	38.97	0.9999	0.200	1447.97
Indoor4	0.5	41.38	0.9983	0.233	271.68
	0.3	40.33	0.9977	0.260	279.67
	0.1	25.60	0.9999	0.515	1797.60
Indoor6	0.5	39.32	0.9998	0.205	1639.61
	0.3	39.00	0.9998	0.220	1655.10
	0.1	36.82	0.9996	0.267	1805.60
Indoor9	0.5	31.85	0.9970	0.336	2053.90
	0.3	31.42	0.9961	0.356	2052.87
	0.1	30.43	0.9936	0.400	2388.33
Outdoor5	0.5	33.90	0.9895	0.510	47.63
	0.3	32.70	0.9868	0.566	50.30
	0.1	31.37	0.9778	0.684	59.97
Outdoor6	0.5	29.86	0.9999	0.332	562.84
	0.3	27.69	0.9998	0.388	603.45
	0.1	25.16	0.9997	0.456	713.15
Outdoor9	0.5	30.99	0.9935	0.5580	52.90
	0.3	30.08	0.9919	0.6093	56.49
	0.1	28.75	0.9879	0.7055	65.89

Table 2: Performance with varying Bit Rate ($r_4 = 1$)

Sequence	PDR (r_4)	PSNR (dB)	SSIM	T_{error}	CR (bit rate)
Indoor3	1	41.71	0.9999	0.197	1048.16
	2	39.52	0.9999	0.230	1117.74
	3	37.91	0.9999	0.257	1158.69
Indoor4	1	40.33	0.9977	0.260	279.67
	2	37.16	0.9954	0.348	290.70
	3	35.22	0.9939	0.398	298.73
Indoor6	1	39.00	0.9998	0.220	1655.10
	2	36.70	0.9996	0.276	1742.88
	3	35.45	0.9995	0.307	1807.72
Indoor9	1	31.42	0.9961	0.356	2052.87
	2	29.49	0.9922	0.424	2117.61
	3	28.38	0.9899	0.461	2159.61
Outdoor5	1	32.70	0.9868	0.566	50.30
	2	30.82	0.9741	0.712	60.40
	3	30.02	0.9661	0.783	69.21
Outdoor6	1	27.69	0.9998	0.388	603.45
	2	23.77	0.9997	0.488	712.75
	3	20.96	0.9996	0.549	794.22
Outdoor9	1	30.08	0.9919	0.609	56.49
	2	27.32	0.9819	0.801	72.00
	3	25.93	0.9742	0.898	86.39

Table 3: Performance with varying r_4 at 0.3 Mbps

increases with an increase of r_4 , indicating the increase of temporal distortion. The compression ratio also increases with an increase of r_4 . Sample event images for the original and compressed events for the Indoor6 sequence (frame 150) is shown in Fig. 2 (row 3) at 100 kbps. With the increase in r_4 , the event image becomes less dense. It is noted that by setting different values of r_4 , we can obtain a target bit rate for the events at a cost of a particular distortion.

6. Comparative Performance measure with other benchmark strategies

The proposed PDS-LEC algorithm is compared with other techniques such as TALVEN [21] and Spike Coding

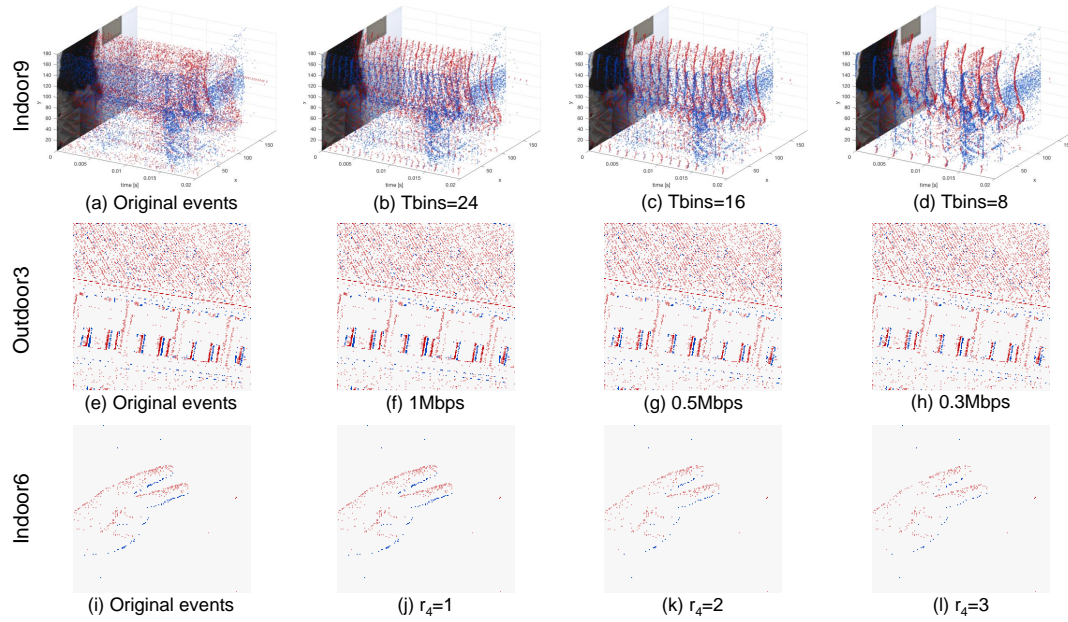


Figure 2: Row 1: temporal binning comparison for Indoor9 (human walking); Row 2: bit rate comparison for Outdoor3 (building) with $r_4 = 1$; Row 3: r_4 comparison for Indoor6 (hand gesture).

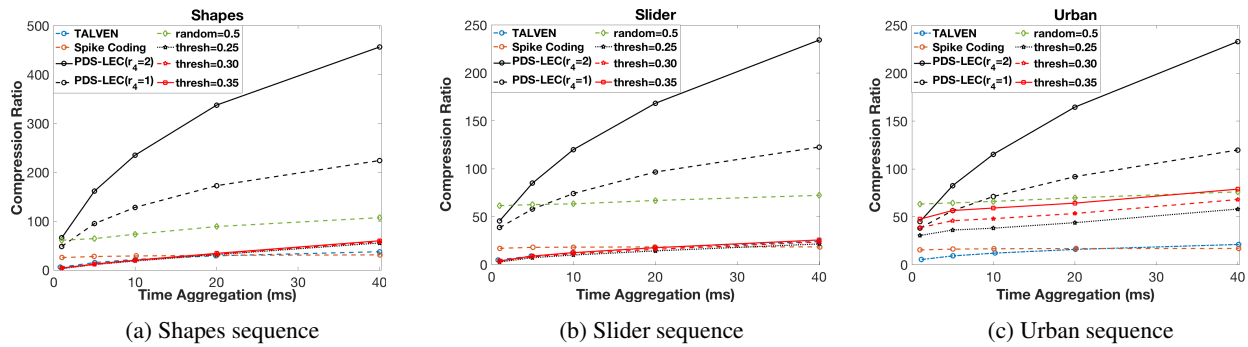


Figure 3: Compression Ratio of PDS-LEC (our work) at 100 kbps, $r_4 = 1, 2$, with TALVEN [21], Spike Coding [16], random (random = 0.5) and CT (thresh = 0.25, 0.30, 0.35) techniques

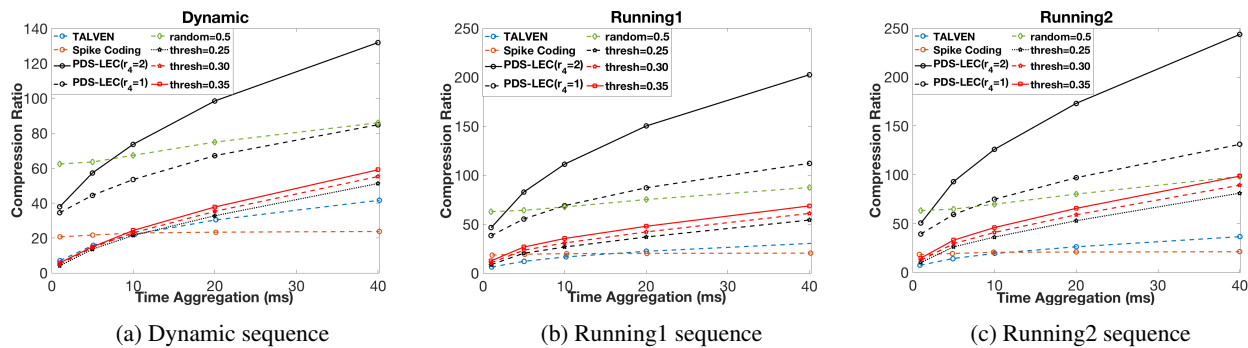


Figure 4: Compression Ratio of PDS-LEC (our work) at 300 kbps, $r_4 = 1, 2$, with TALVEN [21], Spike Coding [16], random (random = 0.5) and CT (thresh = 0.25, 0.30, 0.35) techniques

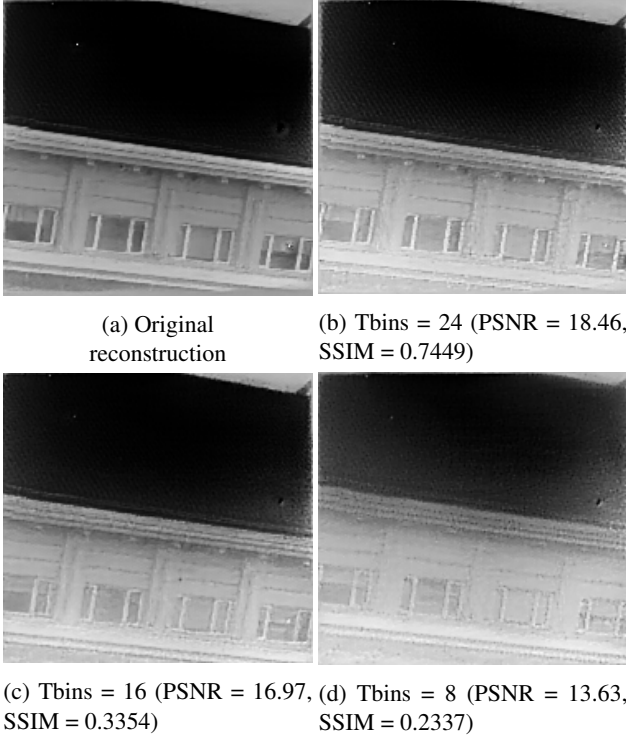


Figure 5: Image reconstruction with encoded events with time duration 33 ms, (Outdoor 3 sequence, Frame 6)

[16] using sequences from DAVIS dataset [29]. In literature, they are the best performing event compression algorithms. In TALVEN, the events are aggregated into positive and negative event frames with histogram count at each pixel location, which are then coded (refer to subsection 2.1). The compression ratio of other algorithms [6, 3] in literature are even lower than TALVEN and Spike Coding [21] and hence not included in the comparative study. Figs. 3 and 4 show the comparative results with different time aggregations. We also compare our method by replacing the QT with 16×16 uniform blocks and PDS by random sampling of 50% of the events followed by temporal aggregation. The rest of the coding strategy in PDS-LEC is followed. Additional comparison is performed by generating fewer events for these sequences by using contrast thresholds (CT) of 0.25, 0.30 and 0.35 in ESIM [32] and apply PDS-LEC by replacing QT with uniform 16×16 blocks and removing PDS step. PDS-LEC outperforms current existing algorithms for different bit rates and PDRs in terms of CR. Even for fewer events generated with higher CT (using our compression scheme), PDS-LEC has better CR. However, for 50% random events (using our compression scheme), at lower temporal aggregation, in a few experiments, CR is higher than PDS-LEC, especially at QT derived at higher bit rates and/or lower PDR since less events are removed. However, SSIM and T_{error} metrics as shown in Table 4 in-

dicating performance comparable or worse than PDS-LEC, due to random removal of events resulting in poor SSIM and T_{error} compared to PDS-LEC (please see additional details in supplementary material). Overall improvement in performance with other state-of-art and other alternative lossy techniques is due to temporal aggregation and priority based sampling of events. QT acts as a priority map for the events. The aggregated timestamps are converted into time frames which result is huge compression. Additionally, differential encoding, HE and RLE further increases CR.

Sequence	method	SSIM, T_{error}				
		1 ms	5 ms	10 ms	20 ms	40 ms
Dynamic	Rn	0.850, 2.211	0.848, 2.222	0.843, 2.248	0.837, 2.406	0.831, 3.128
	PL1	0.986, 0.956	0.937, 1.698	0.905, 1.978	0.871, 2.335	0.845, 3.128
	PL2	0.969, 1.299	0.884, 2.099	0.840, 2.345	0.801, 2.609	0.772, 3.130
	TH25	0.545, 2.409	0.545, 2.183	0.545, 2.070	0.545, 2.228	0.545, 3.127
	TH30	0.558, 2.449	0.558, 2.229	0.558, 2.122	0.558, 2.257	0.558, 3.127
	TH35	0.567, 2.551	0.567, 2.266	0.567, 2.165	0.567, 2.285	0.567, 3.128
Running1	Rn	0.836, 2.467	0.834, 2.461	0.831, 2.467	0.825, 2.648	0.818, 3.491
	PL1	0.968, 1.444	0.894, 2.234	0.852, 2.499	0.816, 2.802	0.790, 3.491
	PL2	0.933, 1.930	0.819, 2.701	0.772, 2.911	0.737, 3.108	0.712, 3.490
	TH25	0.554, 3.213	0.554, 2.841	0.554, 2.593	0.554, 2.619	0.554, 3.491
	TH30	0.574, 3.235	0.574, 2.926	0.574, 2.684	0.574, 2.684	0.574, 3.491
	TH35	0.588, 3.259	0.588, 2.990	0.588, 2.764	0.588, 2.745	0.588, 3.491

Table 4: Comparison of lossy compression techniques. Rn: Random sampling of 50 % events. PL1, PL2: PDS-LEC with $r_4 = 1, 2$ at 0.3 Mbps. TH25, TH30, TH35: Fewer events with CT = 0.25, 0.30, 0.35 respectively.

7. Applications to Image Reconstruction

We used E2VID [33] for reconstruction of images from events. The events are compressed with PDR of $r_4 = 1$ at 300 kbps. Fig. 5(a) shows the reconstruction with original events (without compression), while Fig. 5(b), (c) and (d) shows the reconstruction for $T_{bin} = 24, 16$ and 8. The PSNR and SSIM are computed with respect to the original reconstructed image, Fig. 5(a). Both PSNR and SSIM metrics increases with the increase of T_{bin} , indicating preference of higher T_{bin} for higher image reconstruction quality, with distorted event timestamps closer to actual timestamp.

8. Conclusion and Discussion

The paper proposes a novel lossy event compression algorithm in the spatio-temporal domain based on Poisson disk sampling and time aggregation, which achieves state-of-the-art compression performance. The algorithm uses a QT segmentation of the intensity frames which provides priority regions. We show effectiveness of PDS-LEC in different experiments¹: temporal, spatial, and spatio-temporal binning with comparisons and application to image reconstruction.

¹The readers are encouraged to read the supplementary material.

References

- [1] <https://inivation.com/support/software/fileformat/> Last accessed on April 30, 2020. **1**
- [2] <https://facebook.github.io/zstd/> Last accessed on September 27, 2020. **2**
- [3] <https://www.7-zip.org/sdk.html> Last accessed on April 30, 2020. **3, 8**
- [4] <http://google.github.io/snappy/> Last accessed on September 27, 2020. **3**
- [5] <https://sites.google.com/view/guided-event-filtering> Last accessed on April 30, 2020. **5**
- [6] Jyrki Alakuijala, Andrea Farruggia, Paolo Ferragina, Eugene Kliuchnikov, Robert Obryk, Zoltan Szabadka, and Lode Vandevenne. Brotli: A general-purpose data compressor. *ACM Transactions on Information Systems (TOIS)*, 37(1):1–30, 2018. **3, 8**
- [7] Srutarshi Banerjee, Juan G. Serra, Henry H. Chopp, Oliver Cossairt, and Aggelos K. Katsaggelos. An adaptive video acquisition scheme for object tracking. In *2019 27th European Signal Processing Conference (EUSIPCO)*, pages 1–5. IEEE, 2019. **3, 10**
- [8] Zhichao Bi, Siwei Dong, Yonghong Tian, and Tiejun Huang. Spike coding for dynamic vision sensors. In *2018 Data Compression Conference*, pages 117–126. IEEE, 2018. **1, 2, 3**
- [9] Davis Blalock, Samuel Madden, and John Guttag. Sprintz: Time series compression for the internet of things. *Proceedings of the ACM on Interactive, Mobile, Wearable and Ubiquitous Technologies*, 2(3):1–23, 2018. **3**
- [10] Robert Bridson. Fast poisson disk sampling in arbitrary dimensions. *SIGGRAPH sketches*, 10:1278780–1278807, 2007. **2, 4**
- [11] Andrea Censi and Davide Scaramuzza. Low-latency event-based visual odometry. In *2014 IEEE International Conference on Robotics and Automation (ICRA)*, pages 703–710. IEEE, 2014. **1**
- [12] Robert L Cook. Stochastic sampling in computer graphics. *ACM Transactions on Graphics (TOG)*, 5(1):51–72, 1986. **3**
- [13] Robert L Cook. Stochastic sampling in computer graphics. *ACM Transactions on Graphics (TOG)*, 5(1):51–72, 1986. **3**
- [14] Peter Deutsch and Jean-Loup Gailly. Zlib compressed data format specification version 3.3. Technical report, RFC 1950, May, 1996. **3**
- [15] Alexander Dieckmann and Reinhard Klein. Hierarchical additive poisson disk sampling. In *Proceedings of the Conference on Vision, Modeling, and Visualization*, pages 79–87. Eurographics Association, 2018. **3**
- [16] Siwei Dong, Zhichao Bi, Yonghong Tian, and Tiejun Huang. Spike coding for dynamic vision sensor in intelligent driving. *IEEE Internet of Things Journal*, 6(1):60–71, 2018. **1, 2, 3, 7, 8**
- [17] Robert W Floyd. An adaptive algorithm for spatial grayscale. In *Proc. Soc. Inf. Disp.*, volume 17, pages 75–77, 1976. **3**
- [18] Guillermo Gallego, Tobi Delbruck, Garrick Orchard, Chiara Bartolozzi, Brian Taba, Andrea Censi, Stefan Leutenegger, Andrew Davison, Joerg Conradt, Kostas Daniilidis, et al. Event-based vision: A survey. *arXiv preprint arXiv:1904.08405*, 2019. **2, 3**
- [19] Wen Gao and Siwei Ma. An overview of avs2 standard. In *Advanced Video Coding Systems*, pages 35–49. Springer, 2014. **2**
- [20] Nabeel Khan, Khurram Iqbal, and Maria G Martini. Lossless compression of data from static and mobile dynamic vision sensors-performance and trade-offs. *IEEE Access*, 2020. **3**
- [21] N. Khan, K. Iqbal, and M. G. Martini. Time aggregation based lossless video encoding for neuromorphic vision sensor data. *IEEE Internet of Things Journal*, pages 1–1, 2020. **1, 2, 3, 5, 6, 7, 8**
- [22] Nabeel Khan and Maria G. Martini. Bandwidth modeling of silicon retinas for next generation visual sensor networks. *Sensors (Basel)*, 19(8):1751–1777, 2019. **3**
- [23] Hanme Kim, Stefan Leutenegger, and Andrew J Davison. Real-time 3d reconstruction and 6-dof tracking with an event camera. In *Eur. Conf. Comput. Vis.*, pages 349–364. Springer, 2016. **1**
- [24] Xavier Lagorce, Cédric Meyer, Sio-Hoi Ieng, David Filliat, and Ryad Benosman. Asynchronous event-based multi-kernel algorithm for high-speed visual features tracking. *IEEE transactions on neural networks and learning systems*, 26(8):1710–1720, 2014. **1**
- [25] Matteo Paolo Lanaro, Hélène Perrier, David Coeurjolly, Victor Ostromoukhov, and Alessandro Rizzi. Blue-noise sampling for human retinal cone spatial distribution modeling. *Journal of Physics Communications*, 4(3):035013, 2020. **3**
- [26] Daniel Lemire and Leonid Boytsov. Decoding billions of integers per second through vectorization. *Software: Practice and Experience*, 45(1):1–29, 2015. **3**
- [27] Patrick Lichtsteiner, Christoph Posch, and Tobi Delbruck. A 128×128 120 db 15 μs latency asynchronous temporal contrast vision sensor. *IEEE journal of solid-state circuits*, 43(2):566–576, 2008. **1**
- [28] IS Mostafavi, Jonghyun Choi, and Kuk-Jin Yoon. Learning to super resolve intensity images from events. *IEEE Conf. Comput. Vis. Pattern Recog.*, 2020. **1**
- [29] Elias Mueggler, Henri Rebecq, Guillermo Gallego, Tobi Delbruck, and Davide Scaramuzza. The event-camera dataset and simulator: Event-based data for pose estimation, visual odometry, and slam. *The International Journal of Robotics Research*, 36(2):142–149, 2017. **2, 5, 8, 11, 12**
- [30] Debargha Mukherjee, Jim Bankoski, Adrian Grange, Jingning Han, John Koleszar, Paul Wilkins, Yaowu Xu, and Ronald Bultje. The latest open-source video codec vp9—an overview and preliminary results. In *2013 Picture Coding Symposium (PCS)*, pages 390–393. IEEE, 2013. **2**
- [31] Henri Rebecq, Guillermo Gallego, Elias Mueggler, and Davide Scaramuzza. Emvs: Event-based multi-view stereo—3d reconstruction with an event camera in real-time. *International Journal of Computer Vision*, 126(12):1394–1414, 2018. **1**
- [32] Henri Rebecq, Daniel Gehrig, and Davide Scaramuzza. Esim: an open event camera simulator. In *Conference on Robot Learning*, pages 969–982, 2018. **8, 11**

- [33] Henri Rebecq, René Ranftl, Vladlen Koltun, and Davide Scaramuzza. High speed and high dynamic range video with an event camera. *IEEE Transactions on Pattern Analysis and Machine Intelligence*, 2019. **1, 8**
- [34] Cedric Scheerlinck, Henri Rebecq, Daniel Gehrig, Nick Barnes, Robert Mahony, and Davide Scaramuzza. Fast image reconstruction with an event camera. In *The IEEE Winter Conference on Applications of Computer Vision*, pages 156–163, 2020. **1**
- [35] Guido M Schuster and Aggelos K Katsaggelos. A video compression scheme with optimal bit allocation among segmentation, motion, and residual error. *IEEE Transactions on Image Processing*, 6(11):1487–1502, 1997. **10**
- [36] Guido M Schuster and Aggelos K Katsaggelos. An optimal quadtree-based motion estimation and motion-compensated interpolation scheme for video compression. *IEEE Transactions on image processing*, 7(11):1505–1523, 1998. **3, 11**
- [37] Prasan Shedligeri and Kaushik Mitra. Photorealistic image reconstruction from hybrid intensity and event-based sensor. *Journal of Electronic Imaging*, 28(6):063012, 2019. **1**
- [38] Bongki Son, Yunjae Suh, Sungho Kim, Heejae Jung, Jun-Seok Kim, Changwoo Shin, Keunju Park, Kyoobin Lee, Jinman Park, Jooyeon Woo, et al. A 640×480 dynamic vision sensor with a $9 \mu\text{m}$ pixel and 300Meps address-event representation. In *IEEE International Solid-State Circuits Conference (ISSCC)*, pages 66–67, 2017. **1**
- [39] Gary J Sullivan, Jens-Rainer Ohm, Woo-Jin Han, and Thomas Wiegand. Overview of the high efficiency video coding (hevc) standard. *IEEE Transactions on circuits and systems for video technology*, 22(12):1649–1668, 2012. **2**
- [40] Robert Ulichney. *Digital halftoning*. MIT press, 1987. **3**
- [41] Antoni Rosinol Vidal, Henri Rebecq, Timo Horstschaefer, and Davide Scaramuzza. Ultimate slam? combining events, images, and imu for robust visual slam in hdr and high-speed scenarios. *IEEE Robotics and Automation Letters*, 3(2):994–1001, 2018. **1, 2**
- [42] Florent Wachtel, Adrien Pilleboue, David Coeurjolly, Katherine Breeden, Gurprit Singh, Gaël Cathelin, Fernando De Goes, Mathieu Desbrun, and Victor Ostromoukhov. Fast tile-based adaptive sampling with user-specified fourier spectra. *ACM Transactions on Graphics (TOG)*, 33(4):1–11, 2014. **3**
- [43] Lin Wang, Yo-Sung Ho, Kuk-Jin Yoon, et al. Event-based high dynamic range image and very high frame rate video generation using conditional generative adversarial networks. In *IEEE Conf. Comput. Vis. Pattern Recog.*, pages 10081–10090, 2019. **1**
- [44] Lin Wang, Tae-Kyun Kim, and Kuk-Jin Yoon. Eventsr: From asynchronous events to image reconstruction, restoration, and super-resolution via end-to-end adversarial learning. *IEEE Conf. Comput. Vis. Pattern Recog.*, 2020. **1**
- [45] Zihao Winston Wang, Peiqi Duan, Oliver Cossairt, Aggelos Katsaggelos, Tiejun Huang, and Boxin Shi. Joint filtering of intensity images and neuromorphic events for high-resolution noise-robust imaging. In *IEEE Conf. Comput. Vis. Pattern Recog.*, 2020. **1, 2, 5**
- [46] Zihao Winston Wang, Weixin Jiang, Kuan He, Boxin Shi, Aggelos Katsaggelos, and Oliver Cossairt. Event-driven video frame synthesis. In *Proc. of the IEEE International Conference on Computer Vision (ICCV) Workshops*, 2019. **1**
- [47] Li-Yi Wei. Parallel poisson disk sampling. *ACM Transactions on Graphics (TOG)*, 27(3):1–9, 2008. **3**
- [48] T. Wiegand, G. J. Sullivan, G. Bjontegaard, and A. Luthra. Overview of the h.264/avc video coding standard. *IEEE Transactions on Circuits and Systems for Video Technology*, 13(7):560–576, 2003. **2**
- [49] Lan Xu, Weipeng Xu, Vladislav Golyanik, Marc Habermann, Lu Fang, and Christian Theobalt. Eventcap: Monocular 3d capture of high-speed human motions using an event camera. *IEEE Conf. Comput. Vis. Pattern Recog.*, 2020. **1**
- [50] Dong-Ming Yan, Jian-Wei Guo, Bin Wang, Xiao-Peng Zhang, and Peter Wonka. A survey of blue-noise sampling and its applications. *Journal of Computer Science and Technology*, 30(3):439–452, 2015. **3**
- [51] Cem Yuksel. Sample elimination for generating poisson disk sample sets. In *Computer Graphics Forum*, volume 34, pages 25–32. Wiley Online Library, 2015. **3**
- [52] Alex Zihao Zhu, Nikolay Atanasov, and Kostas Daniilidis. Event-based feature tracking with probabilistic data association. In *2017 IEEE International Conference on Robotics and Automation (ICRA)*, pages 4465–4470. IEEE, 2017. **1**
- [53] Alex Zihao Zhu, Dinesh Thakur, Tolga Özaslan, Bernd Pfrommer, Vijay Kumar, and Kostas Daniilidis. The multivehicle stereo event camera dataset: An event camera dataset for 3d perception. *IEEE Robotics and Automation Letters*, 3(3):2032–2039, 2018. **2**
- [54] Jacob Ziv and Abraham Lempel. A universal algorithm for sequential data compression. *IEEE Transactions on information theory*, 23(3):337–343, 1977. **3**

9. Supplementary Material

9.1. Optimized QT based on rate distortion of Images

Quadtree (QT) may be generated in several ways depending on the system and application. In some works in literature [7], the system is developed as a Host-Chip communication problem in bandwidth-constrained environment, where the QT is developed to compress the grayscale intensity frames. In this work, we use similar system setting in order to generate the QT based on the grayscale intensity frames. For a frame f_t , we have a QT segmentation, skip / acquire modes for the leaves, and values for the leaves of acquire modes, denoted by S_t , Q_t , and V_t , respectively. These are used to reconstruct the frame \hat{f}_t in a remote host, which is distorted version of f_t . The previously reconstructed frame \hat{f}_{t-1} is used to copy the values in the skip leaves of \hat{f}_t , while V_t provides the acquire values of the leaves in S_t .

The full resolution frame f_{t+1} is acquired at time $t + 1$ from the imager. The frames f_{t+1} and \hat{f}_t are inputs to the Viterbi Optimization algorithm [35], which provides the optimal QT structure S_{t+1} and skip-acquire modes Q_{t+1} subject to the bandwidth constraint B (expressed as maximum

bit rate R_{max}). The Viterbi optimization provides a trade-off between the frame distortion and frame bit rate. This is done by minimizing the frame distortion D over the leaves of the QT \mathbf{x} subject to a given maximum frame bit rate R_{max} . The reconstructed frame \hat{f}_t along with frame f_{t+1} is used to compute the distortion at frame $t + 1$.

The optimization is formulated as follows,

$$\begin{aligned} \arg \min_{\mathbf{x}} D(\mathbf{x}), \\ \text{s. t. } R(\mathbf{x}) \leq R_{max} \end{aligned} \quad (\text{S1})$$

The distortion for each node of the QT, \mathbf{x} , is based on the skip-acquire acquisition mode Q_t of that node. If a particular node \hat{x}_t of a reconstructed frame at time t is skip, the distortion with respect to the new node at time $t + 1$, x_{t+1} , is given by

$$D_s = |x_{t+1} - \hat{x}_t|, \quad (\text{S2})$$

On the contrary, if the node is an acquire, the distortion is proportional to the standard deviation σ as shown in Eqn. S3:

$$D_a = \sigma \times 4^{N-n}, \quad (\text{S3})$$

where N is the maximum depth of the QT and n is the level of the QT where distortion is computed. The root and the most subdivided level is defined to be in level 0 and N respectively. The total distortion is therefore defined as:

$$D = D_s + D_a, \quad (\text{S4})$$

The constrained discrete optimization of Eqn. S1 is solved using Lagrangian relaxation, leading to solutions in the convex hull of the rate-distortion curve [36]. The Lagrangian cost function is of the form:

$$J_\lambda(\mathbf{x}) = D(\mathbf{x}) + \lambda R(\mathbf{x}), \quad (\text{S5})$$

where $\lambda \geq 0$ is a Lagrangian multiplier. It has been shown that if there is a λ^* such that

$$\mathbf{x}^* = \arg \min_{\mathbf{x}} J_{\lambda^*}(\mathbf{x}), \quad (\text{S6})$$

which leads to $R(\mathbf{x}^*) = R_{max}$ (within a tolerance), then \mathbf{x}^* is the optimal solution to Eqn. S1. In order to compress the grayscale intensity frames at desired bit-rate in an optimal manner, Lagrangian multiplier (λ) in Eqn. S5 is adjusted in each frame to achieve the desired bit rate. The optimal λ^* is computed by a convex search in the Bezier

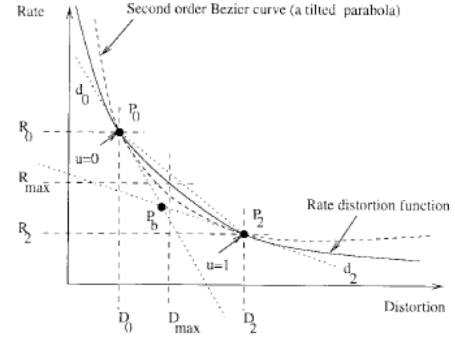


Figure 6: Rate Control using Bezier Curve [36] curve [36]. A sample curve is shown in Fig. 6. In this work, for compressing the events, we consider the events in both the skip-acquire regions of the QT and compress the events depending on the QT block size. However, depending on the application, events in the acquire regions of the QT can be only compressed, while other events can be discarded.

9.2. Comparative Performance

In addition to the summarized results in Section 6 of the main manuscript, we present here additional comparison results using DAVIS dataset [29] sequences: Urban, Shapes, Dynamic, Running1 and Running2. We use our PDS-LEC algorithm with quad tree (QT) generated for 0.1 Mbps and 0.3 Mbps for Poisson Disk Radius (PDR) of $r_4 = 1$ and 2. In addition, the comparison of our algorithm with 50% random event sampling and reduced set of events generated by varying the thresholds to 0.25, 0.30 and 0.35 generated using [32] is shown in Table S1. These are referred to as TH25, TH30 and TH35 in Table S1. We use the same compression strategy as mentioned in Section 6 of the main manuscript. We compare compression ratio (CR), PSNR, SSIM and T_{error} metrics for comparing the performance of the PDS-LEC with other reduced event generation methods. CR, PSNR, SSIM and T_{error} is computed based on the original events provided in the DAVIS dataset [29]. Clearly TH25, TH30 and TH35 have lower PSNR, SSIM, CR and higher T_{error} compared to results generated by PDS-LEC with almost all cases with different PDR and QT generated from different bit rates (PL1r100, PL2r100, PL1r300, PL2r300) as detailed in Table S1. This is seen irrespective of the different temporal binning T_{bin} in the event compression algorithm. However, when considering the results of only TH25, TH30 and TH35, it is seen that the PSNR, SSIM and T_{error} values are highest for TH35 compared to TH25 and TH30. This is an interesting observation, which highlights the fact that at higher contrast threshold (CT), events are fired which identify the significant edges of the scene.

However, for the cases with different CT (TH25, TH30 and TH35), the CR, PSNR, SSIM and T_{error} are worse for all T_{bins} compared to PDS-LEC, thereby suggesting significant difference in structure from the original event

DAVIS [29] sequence. It is also observed for these cases, that for $T_{bin} = 5, 10$ and 20 ms, the T_{error} is lower than $T_{bin} = 1, 40$ ms. For $T_{bin} = 1$ ms, there are fewer events which are aggregated. This suggest that the events generated by varying CT has less structural similarity in time compared to the original events, while progressively aggregating events temporally generates an event volume which has closer resemblance to original event data. However, for $T_{bin} = 40$ ms, T_{error} is higher as all event timestamps are basically quantized into 40 ms, which increases difference between original event timestamps and quantized timestamps.

On the other hand, keeping 50% of the events randomly (Rn) using our compression technique as mentioned in section 6 of the main paper, the CR, PSNR, SSIM and T_{error} metrics are comparable to that obtained by PDS-LEC event compression technique. However, it is seen that for $T_{bin} = 1$ ms, the CR for Rn is higher, alongwith lower SSIM, PSNR and higher T_{error} than PDS-LEC. This indicates that events sampled randomly at $T_{bin} = 1$ ms has less resemblance to original events in the DAVIS dataset. For higher $T_{bins} = 5, 10, 20, 40$ ms, the CR of PDS-LEC is higher than Rn, thereby implying events less than 50% are sampled. However PSNR, SSIM and T_{error} of Rn is comparable to PDS-LEC.

It is observed that for PDS-LEC at 0.1 Mbps with $r_4 = 1, 2$, the CR is higher than that at 0.3 Mbps, with slightly lower SSIM, PSNR and higher T_{error} . Clearly, PDS-LEC offers the flexibility of varying CR, and hence PSNR, SSIM and T_{error} , depending on the bit rate available for transmission and / or storage by varying the PDR (r_4) as demonstrated throughout the paper based on priority given by QT. The algorithm performs better than fewer events generated with varying CT, and comparable with events sampled randomly at 50 %. However, overall, PDS-LEC has better CR and (or) PSNR / SSIM / T_{error} metrics than Rn as seen in Table S1. Moreover, Rn does not offer much flexibility in terms of varying the CR based on available bit rate. Thus PDS-LEC clearly has more potential and flexibility of compressing events in a lossy manner than any other method in literature or other naiive techniques.

Sequence	method	1 ms	5 ms	10 ms	20 ms	40 ms
(CR / PSNR / SSIM / T_{error})						
Urban	Rn	63.35 / 53.01 / 0.9952 / 2.100	64.53 / 53.04 / 0.9952 / 2.111	66.11 / 53.32 / 0.9951 / 2.146	69.89 / 53.17 / 0.9949 / 2.313	76.06 / 53.72 / 0.9947 / 2.970
	PL1r100	38.34 / 65.33 / 0.9987 / 1.172	56.41 / 59.61 / 0.9949 / 1.902	71.24 / 58.13 / 0.9929 / 2.192	91.98 / 57.21 / 0.9913 / 2.468	119.83 / 55.98 / 0.9899 / 2.970
	PL2r100	45.22 / 61.72 / 0.9970 / 1.558	83.10 / 56.90 / 0.9911 / 2.284	116.22 / 55.72 / 0.9889 / 2.515	163.87 / 55.10 / 0.9876 / 2.689	231.97 / 54.53 / 0.9864 / 2.970
	PL1r300	35.09 / 68.22 / 0.9994 / 0.929	46.17 / 62.08 / 0.9969 / 1.627	54.70 / 60.23 / 0.9954 / 1.935	66.15 / 58.92 / 0.9941 / 2.285	81.02 / 57.92 / 0.9930 / 2.970
	PL2r300	38.70 / 64.89 / 0.9984 / 1.240	60.22 / 59.19 / 0.9939 / 1.997	78.00 / 57.68 / 0.9917 / 2.277	102.42 / 56.63 / 0.9901 / 2.540	134.76 / 55.93 / 0.9889 / 2.970
	TH25	30.52 / 45.01 / 0.9813 / 2.906	36.21 / 45.01 / 0.9813 / 2.683	38.15 / 45.01 / 0.9813 / 2.466	43.90 / 45.01 / 0.9813 / 2.381	58.13 / 45.01 / 0.9813 / 2.970
	TH30	38.67 / 45.64 / 0.9832 / 2.918	45.96 / 45.64 / 0.9832 / 2.738	48.11 / 45.64 / 0.9832 / 2.551	53.46 / 45.64 / 0.9832 / 2.445	68.08 / 45.64 / 0.9832 / 2.970
TH35	47.60 / 46.08 / 0.9840 / 2.927	56.61 / 46.08 / 0.9840 / 2.782	59.22 / 46.08 / 0.9840 / 2.625	64.31 / 46.08 / 0.9840 / 2.514	78.91 / 46.08 / 0.9840 / 2.970	
Shapes	Rn	61.11 / 27.79 / 0.9470 / 1.352	64.36 / 27.62 / 0.9458 / 1.360	73.38 / 27.22 / 0.9435 / 1.384	89.05 / 26.68 / 0.9408 / 1.494	107.19 / 26.16 / 0.9386 / 1.914
	PL1r100	48.45 / 30.42 / 0.974 / 1.117	94.88 / 25.91 / 0.9350 / 1.549	128.25 / 25.05 / 0.9220 / 1.637	172.67 / 24.48 / 0.9140 / 1.727	224.08 / 24.09 / 0.9090 / 1.914
	PL2r100	65.99 / 27.72 / 0.9545 / 1.369	161.00 / 24.50 / 0.9139 / 1.710	234.64 / 24.00 / 0.9044 / 1.768	338.39 / 23.68 / 0.8981 / 1.820	457.91 / 23.45 / 0.8944 / 1.914
	PL1r300	40.10 / 37.20 / 0.9906 / 0.724	50.04 / 31.75 / 0.9756 / 1.079	57.33 / 30.54 / 0.9701 / 1.183	71.34 / 29.71 / 0.9660 / 1.386	89.06 / 29.16 / 0.9635 / 1.914
	PL2r300	44.56 / 34.35 / 0.9838 / 0.914	59.35 / 29.56 / 0.9640 / 1.253	68.89 / 28.66 / 0.9576 / 1.344	87.15 / 28.03 / 0.9523 / 1.511	110.42 / 27.62 / 0.9491 / 1.914
	TH25	2.94 / 1.43 / 0.8553 / 1.246	11.22 / 1.43 / 0.8553 / 0.911	18.56 / 1.43 / 0.8553 / 0.856	31.63 / 1.43 / 0.8553 / 1.112	55.46 / 1.43 / 0.8533 / 1.914
	TH30	3.54 / 3.14 / 0.8590 / 1.265	11.33 / 3.14 / 0.8590 / 0.963	19.39 / 3.14 / 0.8590 / 0.886	32.40 / 3.14 / 0.8590 / 1.123	57.57 / 3.14 / 0.8590 / 1.914
TH35	4.14 / 4.59 / 0.8642 / 1.307	12.36 / 4.59 / 0.8642 / 1.007	20.19 / 4.59 / 0.8642 / 0.914	34.22 / 4.59 / 0.8642 / 1.133	59.91 / 4.59 / 0.8642 / 1.914	
Dynamic	Rn	62.45 / 28.55 / 0.8495 / 2.211	63.58 / 28.45 / 0.8479 / 2.222	67.39 / 28.16 / 0.8434 / 2.248	74.97 / 27.76 / 0.8373 / 2.406	86.04 / 27.34 / 0.8309 / 3.128
	PL1r100	38.07 / 34.63 / 0.9717 / 1.300	58.36 / 28.82 / 0.8890 / 2.113	76.54 / 27.32 / 0.8428 / 2.374	105.33 / 26.23 / 0.7989 / 2.643	143.83 / 25.54 / 0.7650 / 3.128
	PL2r100	46.55 / 31.13 / 0.9353 / 1.765	92.93 / 26.52 / 0.8106 / 2.536	132.87 / 25.60 / 0.7651 / 2.721	195.59 / 25.01 / 0.7295 / 2.880	285.71 / 24.62 / 0.7036 / 3.128
	PL1r300	34.55 / 38.08 / 0.9860 / 0.956	44.49 / 31.58 / 0.9375 / 1.698	53.53 / 29.79 / 0.9049 / 1.978	67.20 / 28.51 / 0.8716 / 2.335	84.93 / 27.67 / 0.8448 / 3.128
	PL2r300	37.94 / 34.70 / 0.9694 / 1.299	57.22 / 28.93 / 0.8839 / 2.098	73.62 / 27.58 / 0.8399 / 2.344	98.35 / 26.68 / 0.8016 / 2.609	131.73 / 26.09 / 0.7723 / 3.130
	TH25	4.12 / 3.66 / 0.545 / 2.409	13.63 / 3.66 / 0.545 / 2.183	21.49 / 3.66 / 0.545 / 2.070	32.78 / 3.66 / 0.545 / 2.228	51.24 / 3.66 / 0.545 / 3.127
	TH30	4.97 / 5.34 / 0.5580 / 2.449	14.61 / 5.34 / 0.5580 / 2.229	23.03 / 5.34 / 0.558 / 2.122	35.27 / 5.34 / 0.558 / 2.257	55.25 / 5.34 / 0.558 / 3.127
TH35	5.83 / 6.790 / 0.5670 / 2.551	14.94 / 6.790 / 0.5670 / 2.266	24.38 / 6.790 / 0.5670 / 2.165	37.79 / 6.790 / 0.5670 / 2.285	59.12 / 6.790 / 0.5670 / 3.128	
Running1	Rn	62.87 / 29.20 / 0.8361 / 2.467	64.14 / 29.13 / 0.8346 / 2.461	67.61 / 28.91 / 0.8308 / 2.467	75.19 / 28.51 / 0.8247 / 2.6480	87.49 / 28.10 / 0.8176 / 3.491
	PL1r100	44.09 / 32.49 / 0.9450 / 1.808	74.54 / 28.06 / 0.8457 / 2.587	99.74 / 26.94 / 0.7977 / 2.822	133.89 / 26.19 / 0.7589 / 3.047	179.75 / 25.70 / 0.7308 / 3.491
	PL2r100	58.51 / 29.66 / 0.893 / 2.309	125.89 / 26.38 / 0.768 / 2.978	182.73 / 25.66 / 0.7239 / 3.141	263.88 / 25.21 / 0.6924 / 3.276	373.98 / 24.95 / 0.6714 / 3.491
	PL1r300	38.38 / 35.14 / 0.9678 / 1.444	55.31 / 29.94 / 0.8942 / 2.234	68.95 / 28.52 / 0.8522 / 2.499	87.22 / 27.58 / 0.8165 / 2.802	112.18 / 26.86 / 0.7895 / 3.491
	PL2r300	45.82 / 32.08 / 0.933 / 1.930	82.57 / 27.62 / 0.8200 / 2.697	110.74 / 26.64 / 0.7727 / 2.907	149.38 / 26.03 / 0.7373 / 3.107	201.25 / 25.65 / 0.7123 / 3.490
	TH25	8.70 / 7.32 / 0.5540 / 3.213	20.34 / 7.32 / 0.5540 / 2.841	26.71 / 7.32 / 0.5540 / 2.593	36.95 / 7.32 / 0.5540 / 2.619	54.26 / 7.32 / 0.5540 / 3.491
	TH30	10.62 / 8.94 / 0.5740 / 3.235	23.43 / 8.94 / 0.5740 / 2.926	30.88 / 8.94 / 0.5743 / 2.684	42.15 / 8.94 / 0.5743 / 2.684	61.00 / 8.94 / 0.5740 / 3.491
TH35	12.59 / 10.274 / 0.5880 / 3.259	26.71 / 10.274 / 0.5880 / 2.990	35.41 / 10.274 / 0.5880 / 2.764	47.89 / 10.274 / 0.5880 / 2.745	68.68 / 10.274 / 0.5880 / 3.491	
Running2	Rn	63.34 / 26.54 / 0.803 / 3.372	64.87 / 26.40 / 0.801 / 3.349	69.87 / 26.14 / 0.7940 / 3.336	80.22 / 25.73 / 0.7850 / 3.570	98.28 / 25.19 / 0.7740 / 4.768
	PL1r100	45.84 / 29.20 / 0.9199 / 2.607	80.20 / 24.92 / 0.7936 / 3.662	109.25 / 23.96 / 0.7380 / 3.890	149.63 / 23.32 / 0.6960 / 4.152	208.91 / 22.85 / 0.6660 / 4.768
	PL1r300	39.91 / 31.93 / 0.9505 / 2.130	59.29 / 26.83 / 0.8516 / 3.168	74.89 / 25.62 / 0.801 / 3.464	96.99 / 24.79 / 0.7611 / 3.822	131.14 / 24.15 / 0.7303 / 4.768
	PL2r300	50.46 / 28.09 / 0.8951 / 2.869	93.00 / 24.31 / 0.7523 / 3.810	126.03 / 23.55 / 0.7003 / 4.031	173.41 / 23.06 / 0.6635 / 4.258	244.27 / 22.71 / 0.6393 / 4.768
	TH25	10.27 / 7.59 / 0.5194 / 4.396	26.13 / 7.59 / 0.5194 / 3.913	36.21 / 7.59 / 0.5194 / 3.612	52.94 / 7.59 / 0.5194 / 3.664	81.19 / 7.59 / 0.5194 / 4.768
	TH30	12.48 / 9.21 / 0.5341 / 4.425	29.49 / 9.21 / 0.5341 / 4.018	40.97 / 9.21 / 0.5341 / 3.724	59.06 / 9.21 / 0.5341 / 3.736	89.38 / 9.21 / 0.5341 / 4.768
	TH35	14.72 / 10.539 / 0.5436 / 4.458	33.07 / 10.539 / 0.5436 / 4.098	45.95 / 10.539 / 0.5436 / 3.821	65.63 / 10.539 / 0.5436 / 3.812	98.65 / 10.539 / 0.5436 / 4.768

Table S1: Comparison of Compression Ratio (CR), PSNR, SSIM and T_{error} for various lossy compression techniques. Rn: Random sampling of 50% events. PL1r100: PDS-LEC with $r_4 = 1$ at 0.1 Mbps. PL2r100: PDS-LEC with $r_4 = 2$ at 0.1 Mbps. PL1r300: PDS-LEC with $r_4 = 1$ at 0.3 Mbps. PL2r300: PDS-LEC with $r_4 = 2$ at 0.3 Mbps. TH25: Fewer events with CT = 0.25. TH30: Fewer events with CT = 0.30. TH35: Fewer events with CT = 0.35.